AIAA 96-2780

Design of a Subscale Propellant Slag Evaluation Motor Using Two-Phase Fluid Dynamic Analysis

R. Harold Whitesides, Richard A. Dill, and David C. Purinton
ERC, Incorporated
Huntsville, AL

Jay K. Sambamurthi
NASA/Marshall Space Flight Center
Huntsville, AL

32nd AIAA/ASME/SAE/ASEE Joint Propulsion Conference

July 1-3, 1996 / Lake Buena Vista, FL

DESIGN OF A SUBSCALE PROPELLANT SLAG EVALUATION MOTOR USING TWO-PHASE FLUID DYNAMIC ANALYSIS

R. Harold Whitesides*, Richard A. Dill**, and David C. Purinton***
ERC, Incorporated, Huntsville, AL

Jay K. Sambamurthi†
NASA Marshall Space Flight Center, Huntsville, AL

Abstract

Small pressure perturbations in the Space Shuttle Reusable Solid Rocket Motor (RSRM) are caused by the periodic expulsion of molten aluminum oxide slag from a pool that collects in the aft end of the motor around the submerged nozzle nose during the last half of motor operation. It is suspected that some motors produce more slag than others due to differences in aluminum oxide agglomerate particle sizes that may relate to subtle differences in propellant ingredient characteristics such as particle size distributions or processing variations. A subscale motor experiment was designed to determine the effect of propellant ingredient characteristics on the propensity for slag production. An existing 5 inch ballistic test motor was selected as the basic test vehicle. The standard converging/diverging nozzle was replaced with a submerged nose nozzle design to provide a positive trap for the slag that would increase the measured slag weights. Two-phase fluid dynamic analyses were performed to develop a nozzle nose design that maintained similitude in major flow field features with the full scale RSRM. The 5 inch motor was spun about its longitudinal axis to further enhance slag collection and retention. Two-phase flow analysis was used to select an appropriate spin rate along with other considerations, such as avoiding burn rate increases due to radial acceleration effects. Aluminum oxide particle distributions used in the flow analyses were measured in a quench bomb for RSRM type propellants with minor variations in ingredient characteristics. Detailed predictions for slag accumulation weights during motor burn compared favorably with slag weight data taken from defined zones in the subscale motor and nozzle. The use of two-phase flow analysis proved successful in gauging the viability of the experimental program during the planning phase and in guiding the design of the critical submerged nose nozzle.

Introduction

Background

In past firings of the Space Shuttle Reusable Solid Rocket Motor (RSRM), both static test and flight motors have shown small pressure perturbations occurring primarily between burn times of 65 and 80 seconds. Considerable variability of the amplitude and duration of the pressure perturbations has been observed. A joint NASA/Thiokol team investigation[1] concluded that the cause of the pressure perturbations was the periodic expulsion of molten aluminum oxide slag from a pool that collects in the aft end of the motor around the submerged nozzle nose during the last half of motor operation. It is suspected that some motors produce more slag than others due to differences in aluminum oxide agglomerate particle sizes that are leaving the burning propellant surface. Variations in the aluminum oxide particle sizes affect the particle trajectories and determine whether particles fly out the nozzle or impact the aft case or underneath structures of the submerged nozzle where they may collect and form a molten slag pool. These variations in aluminum oxide particle sizes may relate to subtle differences in propellant ingredient characteristics such as ammonium perchlorate particle size/distribution, aluminum particle size/distribution/coating and storage, handling or processing variations including humidity effects. Such relationships have been explored by numerous combustion researchers including Sambamurthi[2]. Therefore, it was recognized that variations in specific propellant ingredient characteristics, while

* Manager, Propulsion; AIAA Associate Fellow
** Senior Staff Specialist
*** Senior Engineer
† AST, ED32, AIAA Senior Member

they might be within the material or processing specifications, could lead to increased slag generation in the RSRM. Due to the size of the motor and the propellant mixes, an experimental program based on full scale firings was not feasible. There was a need then, to find a low cost, rapid turn-around experimental device capable of measuring the relative propensity for slag production of the RSRM propellant with minor ingredient variations.

Objectives

Combustion quench bombs, small subscale motors and large subscale motors were considered as test devices to measure the relative slag production propensity for various propellant modifications. A quench bomb measures the relative combustion particle size distributions, which might relate to slag production but it is not a very direct measurement of slag production and entrapment in a motor environment. Large subscale motor tests were too expensive and time consuming to test the desired number of propellant ingredient characteristics. A small subscale motor test was viewed as the best alternative since direct measurements of slag could be made although it is recognized that the percentage amounts of slag trapped are dependent on both the propellant characteristics and the particular motor design. Accordingly, the principal objective of the effort became the development of a small subscale motor test that would be capable of measuring the relative propensity for slag production of the RSRM propellant with small changes in propellant ingredient characteristics. This implies a requirement that the test have the degree of sensitivity, accuracy and reproducibility to accomplish this objective. A secondary objective was to develop a data base on both the total weight and distribution of the accumulated slag in a subscale motor to facilitate validation of a two-phase computational fluid dynamics (CFD) analysis code. It is recognized that "calibration" of the CFD code to the subscale motor may not necessarily qualify it for making accurate predictions of slag accumulation in a motor as large as the RSRM. This secondary objective requires that quench bomb data on the combustion particle distributions and aluminum content also be measured for each mix prepared for subscale motor testing. This paper will address the application of the two-phase fluid dynamics analysis to the design of the test motor, selection of the motor test conditions and analysis of the slag accumulation data. The selection of propellant ingredient variables for testing and the development of the design-of-experiments test matrix is described in a JANNAF paper by Miks and Allen[3].

Approach

Motor Design

The basic approach revolved around the use of a standard ballistic test motor and spin stand at Thiokol which had previously been used to develop propellants with reduced sensitivity of burn rate to radial acceleration environments. The motor design, test program and experimental test results are thoroughly covered in a companion paper by Perkins[4], et. al. The motor is a cylindrical port design containing a propellant grain with a 5.0 inch outer diameter, a 3.0 inch port diameter, a 1.0 inch web and a 9.0 inch length as shown in Figure 1. A spin stand is available to spin the motor about the longitudinal axis. The capability to spin the small ballistic test

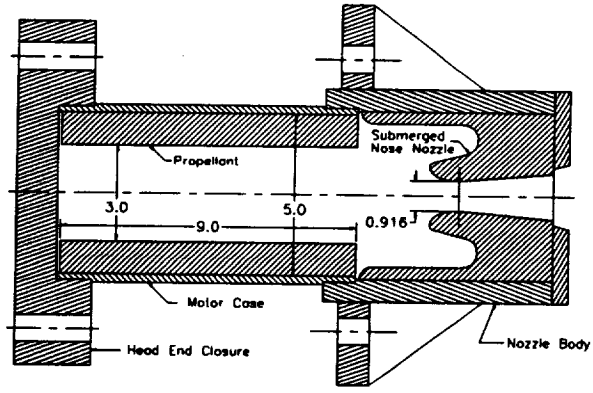

Figure 1. Five Inch Spin Motor Assembly

motor was of interest for two primary reasons: 1) to induce a radial acceleration force on the particulates in the flow thereby increasing the quantity of particle impacts on the nozzle and consequently the post test measured slag weight and 2) to aid in retaining the slag in the motor chamber during tail-off when the rapid depressurization tends to dislodge and expel collected quantities of slag. The initial concern was that collected slag weights would be so small that the required resolution and reproducibility of the experiment would not be realized. However, it was recognized that it would be undesirable to spin the motor at a rate that would substantially change the basic aluminum agglomeration processes on the burning surface in a way that would not be representative of the full scale motor. This concern was satisfied by selecting a

spin rate that resulted in radial accelerations below the threshold value for burn rate augmentation as measured in the motor. The standard converging-diverging nozzle used on the 5 inch ballistic test motor was replaced by a submerged nose nozzle, also shown in Figure 1, to enhance both slag capture during motor operation and slag retention during tailoff. Graphite was chosen for its high thermal diffusivity as the nozzle insert material in order to facilitate the freezing and retention of slag on the surface of the nozzle. The short burn time of the motor also precluded remelting and flowing of the slag on the nozzle surfaces. A nominal subscale motor operating pressure of 600 psia was selected such that the burn rate and agglomeration processes on the propellant surface would replicate those in the full scale motor.

Fluid Dynamic Analysis

The use of two-phase computational fluid dynamic analysis played a major role in the design of this experiment. CFD tools were used during the critical design phase of this project to determine the viability of the experiment, to aid in the design of the motor nozzle and to support selection of the motor test conditions. A priori CFD predictions were made of accumulated slag weights in the 5 inch spin motor using combustion particle size distributions measured for two representative RSRM propellant mixes manufactured with ammonium perchlorate from two different sources. The aluminum oxide particle size distributions for the two propellant samples were measured in the Thiokol quench bomb and found to vary with the average particle size of the ammonium perchlorate. The CFD code predicted measurably higher slag weights for the propellant with the slightly coarser ammonium perchlorate particle size distribution which established credibility that the spin motor test would be able to discriminate between propellants with small changes in ingredient characteristics.

The design approach also included the use of two-phase CFD to evaluate candidate submerged nose nozzle geometries for 1) simulation of the primary flow features in the separated flow region around the submerged nose of the RSRM and for 2) slag capturing and retention characteristics. The plans also included the use of CFD to evaluate the effect of motor spin rate on total accumulated slag weight to aid in selection of a test spin rate. Post-test analysis plans included the use of CFD to evaluate the slag weight and distribution data and also to evaluate a proposed slag capture criteria based on the flow attachment point underneath the nozzle nose. Simply stated, this slag capture criteria assumes that all particles that impact behind the flow attachment point are retained on the wall as accumulated slag and all particles that impact in front of the flow attachment point are swept out of the nozzle. This criteria, if proven valid in the subscale motor, would provide a means to apply the results of this effort to predictions of slag accumulation in the full scale RSRM although the accuracy of the predictions would be unknown until further verification.

Spin Motor Design Analysis

CFD Methodology

The reacting, two-phase flow in the chamber and nozzle of the spin test motor was calculated with the CELMINT[5] (Combined Eulerian Lagrangian Multidimensional Implicit Navier-Stokes Time-dependent) code which considers the flow to consist of two phases. The continuous phase is composed primarily of the gaseous products of combustion from the binder and the ammonium perchlorate. The particulate or discrete phase is composed of molten particles containing both unburned aluminum and aluminum oxide. The combustion of aluminum produces a bi-modal particle size distribution including micron sized aluminum oxide smoke particles which are added to the continuous phase and coarser particulates from burning aluminum agglomerates which form the discrete phase.

CELMINT is a fully implicit, density-based code which solves the ensemble-averaged Navier-Stokes equations (including the continuity, momentum, energy, species transport, and turbulence model equations) with discrete phase mass, momentum, and energy interchange source terms determined from the Lagrangian discrete phase transport calculations. The governing Eulerian equations are written in a general nonorthogonal, body-fitted, axisymmetric coordinate system. The governing partial differential equations are formulated in conservation form and are solved using a consistently split, linearized block-implicit numerical scheme developed by Briley and McDonald[6]. The solution procedure also treats equation nonlinearities non-iteratively by Taylor series linearization in time. The resulting system of multidimensional, coupled, linear difference equations for the dependent

variables is solved using alternating direction implicit techniques which produce an easily solved narrow block-banded subsystem of equations.

Several specialized physical models were used to perform the CFD calculations required for this investigation. The turbulence model is the transitional two-equation model with modifications discussed by Sabnis[7] et al for injection driven flows. The diffusion controlled distributed combustion of the aluminum droplets as they travel down the motor port is treated by using the Hermsen[8] aluminum burn rate correlation. The corresponding gas phase reactions are calculated using chemical equilibrium. The CELMINT code employs a particle fragmentation model based on the critical Weber number approach modified by Hunter[9] et al. A particle agglomeration model which considers the growth of discrete phase particles due to collisions with the fine smoke particles was also incorporated into the CELMINT code. This agglomeration model is based on the experimental observations of Salita[10]. CELMINT uses a highly flexible particle injection model which is crucial to the realistic simulation of flows with particle injection. The code allows particle properties (temperature, size distribution, composition, etc.) to be arbitrarily specified.

Design Analysis Results

In designing the submerged nose nozzle for the 5 inch spin motor, it was desired to achieve similarity in nozzle nose geometry and, in particular, similarity of the major flow field features around the nozzle nose between the subscale motor and the RSRM. This was due to the desire to have the combustion particulates captured and trapped by the subscale motor in the same way as for the full scale motor. This would increase the fidelity of the simulation for the subscale motor slag capturing test and also lend some credibility to efforts to extend the CFD analysis for the subscale motor to the full scale RSRM. The major flow field features around the nose of the RSRM are shown in the Figure 2 velocity vector plot. The flow separates from the propellant grain surface upstream of the nozzle nose and reattaches to the nozzle nose on the underneath surface just aft of the nose tip. A dividing streamline separates a recirculation region underneath the nozzle nose from the approaching flow which sweeps out the nozzle. Just underneath the nozzle nose tip is a high intensity particle impact zone. The flow velocity along the surface underneath the nozzle is aftward which serves to sweep the molten slag layer formed from the impinging particles into the aft cavity where it accumulates as a molten slag pool in the RSRM. These same basic flow features were achieved for the subscale motor as shown in the Figure 3 velocity vector plot. It was found in evaluating several candidate designs that the degree of submergence of the nozzle and the slope of the surface underneath the nose were very influential in determining the direction of the

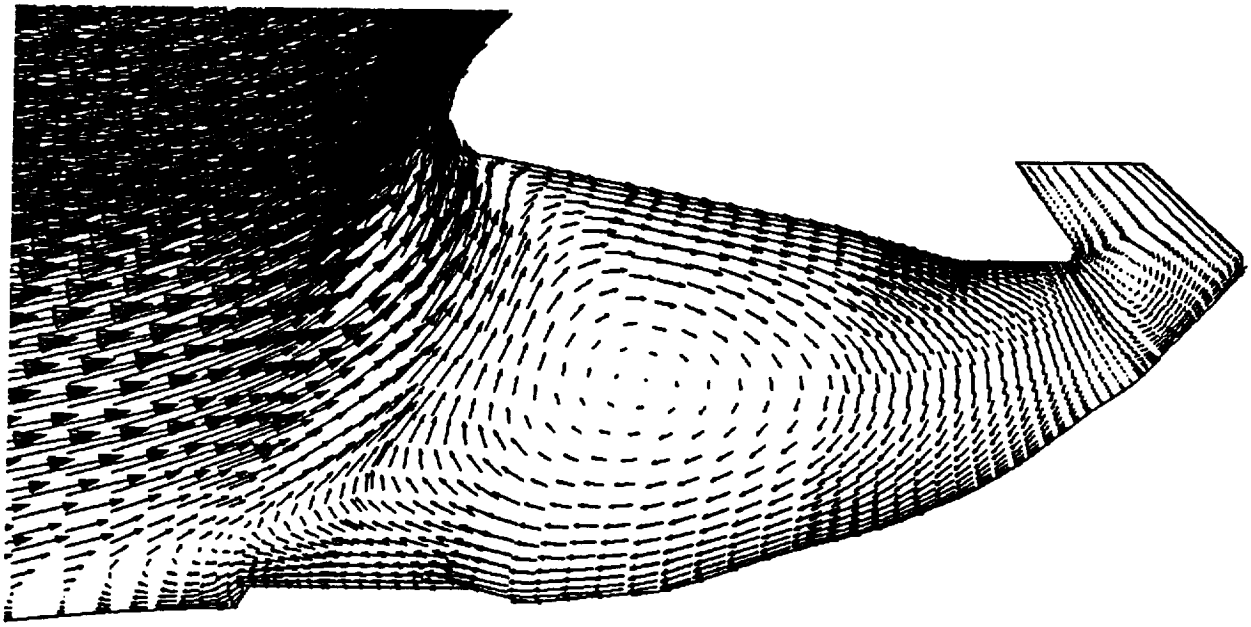

Figure 2. RSRM Aft Cavity Flowfield

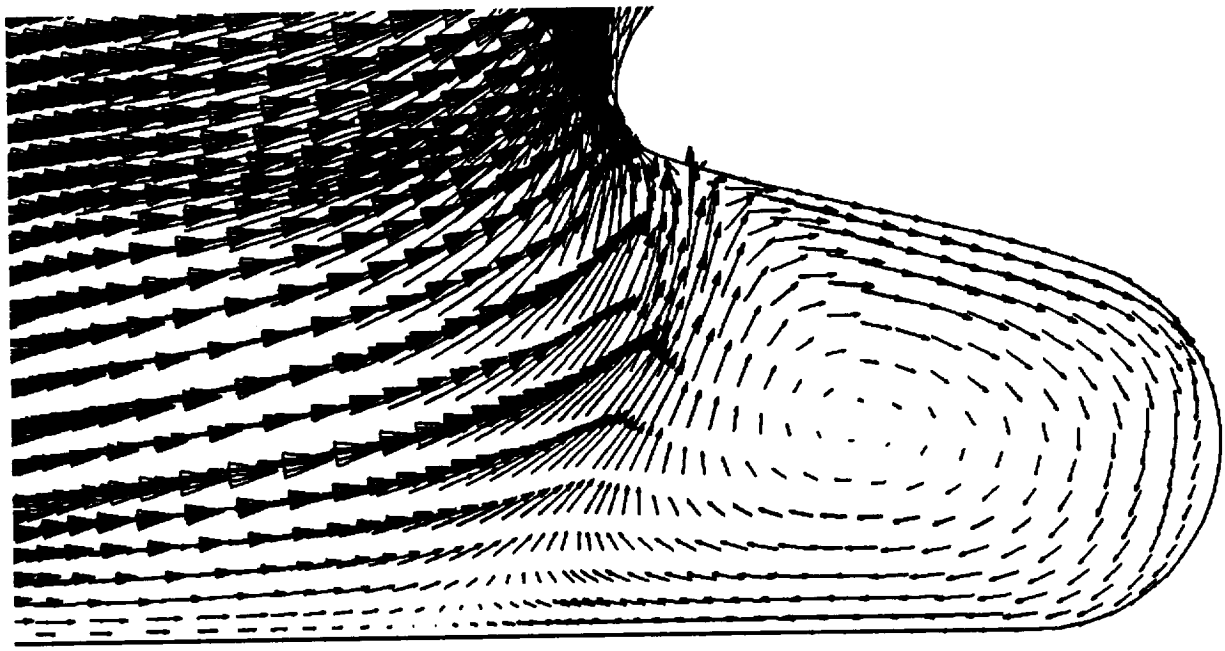

Figure 3. Spin Motor Aft Cavity Flowfield

flow in the recirculation region. Shallow submergence and higher slopes for the underneath nozzle surface would reverse the direction of the flow underneath the nozzle nose to a counterclockwise direction which could serve to reduce the amount of slag captured. It was deemed important to achieve the clockwise rotation of the flow as shown in Figure 3 to replicate conditions in the full scale RSRM.

Fluid dynamic analysis was also used in the initial planning of the experiment to evaluate the effect of motor spin about the longitudinal axis on the quantity of slag captured. It was desired to maximize the weight of slag collected to enhance the accuracy of the experiment. The two-phase CFD code was used to calculate the effect of spin induced radial body forces on particle trajectories and impacts with the nozzle. The particle impacts were integrated over the nozzle surfaces with time to yield both local and total slag capture weights. A plot of the instantaneous slag accumulation rate as a function of spin rate is shown in Figure 4 for the 50 percent web burn time. The nonlinear effect of spin rate results in very little increase in slag accumulation rates at 100 and 200 rpm, but at 300 and 400 rpm the slag accumulation rate increases begin to become significant. The total slag accumulation as a function of burn time is shown in Figure 5 for spin rates of 0 and 400 rpm.

The effect of spin rate on slag accumulation is

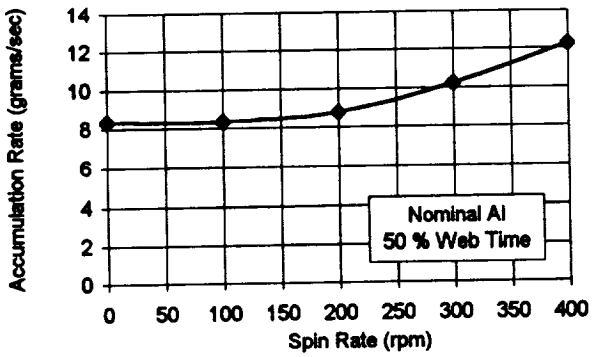

Figure 4. Slag Accumulation Rate

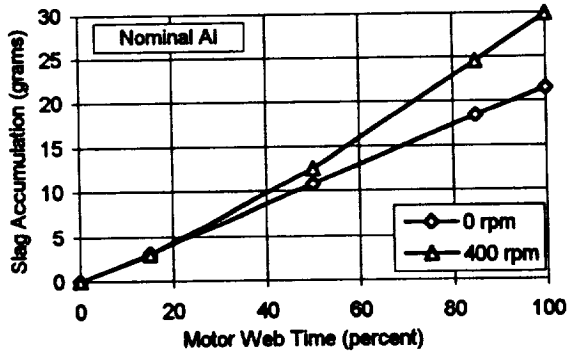

Figure 5. Total Slag Accumulation

seen to increase with burn time. Figure 6 shows the ratio of the slag accumulation rates at 400 and 0 rpm as a function of percent web time. At the end of motor burn an increase of 39 percent in slag weight at 400 rpm over the zero spin case is predicted. This compares favorably with a later obtained experimental value of approximately 43 percent also plotted in Figure 6. Thus it appeared from these early predictions that there would be an obvious advantage to testing at 400 rpm provided that no spin rate induced burning rate augmentation was detected.

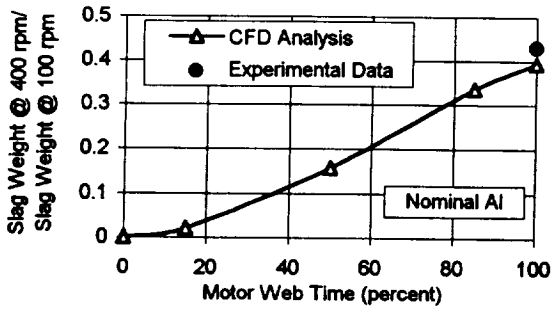

Figure 6. Slag Weight Ratio versus Web Time

Spin Motor Test Analysis

Particle Size Distribution for Selected Mixes:

As part of the primary spin motor test series referenced earlier, a sub-series[11] consisting of six different formulations of the RSRM TP-H1148 production propellant was conducted where the only variation was the ingredient aluminum particle size distribution. This was accomplished by passing the nominal (as-received) aluminum sequentially through a series of sieves and combining and sorting the sieved particles in a predetermined manner. The sequential removal of coarser particles from the nominal aluminum resulted in finer aluminum particles in six subsequent formulations. Based on these formulations, a series of spin motor tests was conducted to study the effect of ingredient aluminum particle size on spin motor slag accumulation. These six formulations were also tested in the particle quench bomb at the Thiokol Corporation Wasatch Facility to develop a correlation between the results of the agglomerate particle size distribution from the quench bomb and the accumulated nozzle slag in the spin motor tests. The quench bomb tests were conducted at 500 psi chamber pressure and the particles in the combustion zone were quenched at 0.5 inch from the burning surface. The size distributions of the collected particles were determined by Microtrac analysis. Three tests under similar test conditions were performed for each formulation. The average of these three tests described the final size distribution of the quenched particles for each formulation. The resulting distributions were primarily bi-modal in nature with 50-70% of the particles by weight being under 5 microns and designated as the "smoke" fraction. The rest of the fraction in the 5-700 micron range was designated as the "coarse" fraction which comprises the discrete fraction in the two-phase CFD analysis. The results of this investigation are presented in detail in a companion paper by Brennan[12].

To generate the size distribution of the quenched particles in the discrete fraction as an input to the CFD analysis in the current investigation, quench bomb results from three of the six propellant formulations were selected. The ingredient aluminum particle size distribution in these three formulations included fine, nominal, and coarse aluminum. For the formulation with fine aluminum, the size distribution of the quenched particles in one of the three repeat tests deviated significantly from the other two tests, hence the results of this test were omitted in the averaging to obtain the final distribution. The cumulative mass fraction of quenched particles in the discrete fraction was 0.3866 for the formulation with fine aluminum, 0.4644 for the formulation with nominal aluminum and 0.4842 for the formulation with coarse aluminum. For any given formulation, a single curve fit through this distribution was not sufficient to provide adequate resolution for the inputs to the CFD calculations. Consequently, the distribution was divided into different zones based on the slope changes in the measured distribution curve and independent polynomial curve fits were generated for each zone such that the R-square values were maintained above 0.99 for each fit. A typical comparison of the polynomial fits with the measured data for the nominal aluminum is shown in Figure 7 which clearly indicates the high accuracy of the fits in describing the measured particle size distribution. The curve fit equations for each of the formulations require several pages and are not included in this paper. The curve fits of the measured cumulative mass fraction distributions for each of the above three formulations are given in Figure 8. It can be seen that the coarser aluminum in the propellant tends to produce higher fractions of the coarser particles in the quench bomb.

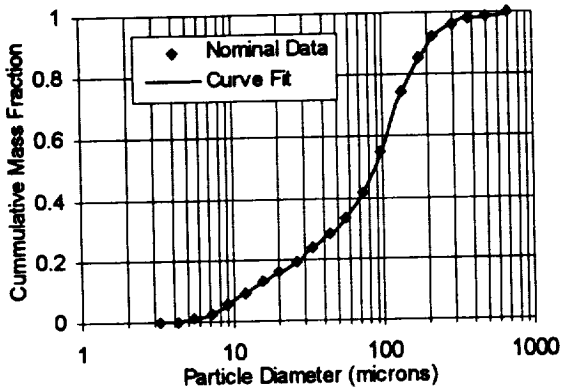

Figure 7. Quench Bomb Data and Polynomial Fits

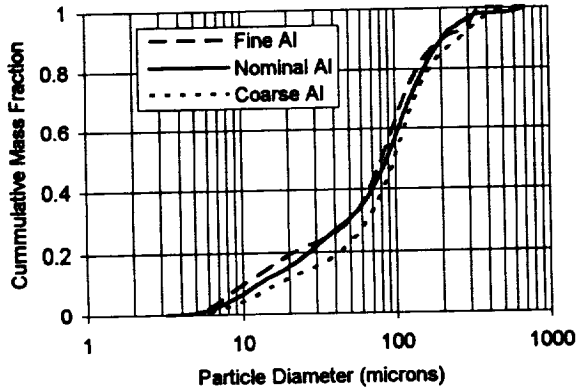

Figure 8. Comparison of Particle Distribution Data

Boundary Conditions

Two-phase CFD predictions were performed for motors loaded with each of the three propellant mixes described in the foregoing section. Each motor was analyzed for three burn times corresponding to 15, 50 and 85 percent web time. This required a total of nine CFD solutions, each with different boundary conditions. Slag accumulation rates for each burn time were integrated to determine the total predicted slag weight at the end of motor burn. The analyses were performed with axisymmetric geometry but with additional body force terms added to account for the centrifugal acceleration generated by the motor spin rate. Thus the calculated flowfield had a circumferential swirl velocity component in addition to the radial and axial components. The computation of the discrete phase particle trajectories was also performed in three dimensions.

The geometry of the propellant surface at each of the three burn times analyzed is shown in Figure 9. The computational grid resolution for each burn time is listed in Table I. A summary of the motor operating conditions at each burn time analyzed is shown in Table II for the nominal aluminum propellant. A representative pressure trace for the spin motor is shown in Figure 10 also for the nominal aluminum propellant. The throat diameter is held constant at 0.916 inches over the web burn time of 2.76 seconds. The computational domain extended through the choked throat downstream to the nozzle exit where an extrapolated supersonic boundary condition was applied. The total motor mass flow rates for each burn time, as listed in Table II, were used to determine the mass injection rates at the surface of the propellant grain. The propellant injection rate was applied normal to the burning surfaces with a no-tangential-slip boundary condition.

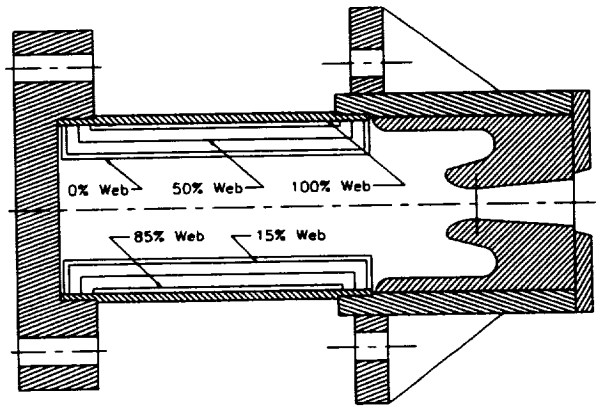

Figure 9. Propellant Burn Back Contours

Table I. Computational Grid Resolution

Location	15% Web	50% Web	85% Web
Port	50 x 50	50 x 65	50 x 65
Nozzle Closure	105 X 85	110 x 95	115 x 80

Table II. Spin Motor Operating Conditions

Parameter	15% Web	50% Web	85% Web
Chamber Pressure	554.2 psia	639.8 psia	579.8 psia
Mass Flow Rate	2.44 lbm/sec	2.82 lbm/sec	2.55 lbm/sec
Propellant Burning Area	112.36 sq. in.	114.67 sq. in.	112.36 sq. in.

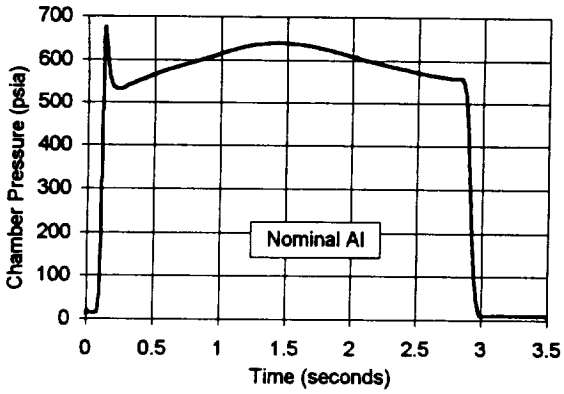

Figure 10. Spin Motor Pressure versus Time

The equilibrium thermochemical parameters, including the condensed phase fraction, Al_2O_3, for the RSRM TP-H1148 propellant are listed in Table III at each of the burn times analyzed. As previously mentioned, the actual thermodynamic properties are changing down the motor port due to the burning of the aluminum droplets in the flowfield. The mass injection boundary conditions at the burning propellant surface for the discrete phase particulates are listed in Table IV. The aluminum oxide particle density used is the combustion flame temperature value for the fully burned particles. The aluminum oxide caps fraction is the fraction of aluminum that is converted to the large Al_2O_3 particle discrete phase during the aluminum combustion process. The remainder is converted to the micron sized smoke particles which are considered part of the continuous phase. The chosen value of 0.2833 for the caps fraction is taken from an analysis of quench bomb data for a representative mix of TP-H1148 propellant at the relatively large quench distance of 3 inches where combustion is nearly complete. The bi-modal particle size distribution data is shown in Figure 11 which shows that the large particle discrete phase is 28.33 percent of the total particle weight.

Table III. RSRM Propellant Thermochemistry*

Parameter	15% Web	50% Web	85% Web
Pressure	554.2 psia	639.8 psia	579.8 psia
Total Temp.	6079 °R	6101 °R	6086 °R
Molecular Weight	28.34	28.38	28.35
Dynamic Viscosity	6.181×10^{-5} lbm/ft-sec	6.192×10^{-5} lbm/ft-sec	6.185×10^{-5} lbm/ft-sec
Ratio of specific heats	1.136	1.137	1.136
Fraction of Al_2O_3	28.75%	28.77%	28.76%

**Propellant TP-H1148 composition is 16% aluminum, 69.7% ammonium perchlorate, 14% PBAN binder and 0.3% iron oxide.*

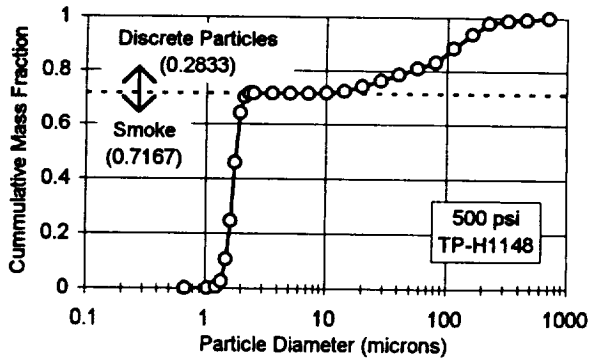

Figure 11. Quench Bomb Particle Data

The surface discrete phase fraction in Table IV is the fraction of the total condensed phase species (including the smoke and any unburned aluminum) that is contained in the burning agglomerated particles leaving the propellant surface. These agglomerated particles are composed of both unburned aluminum and aluminum oxide. Thus when combustion of the aluminum is complete, the local discrete phase fraction becomes equal to the aluminum oxide caps fraction. The Table IV values for the local discrete phase fraction at the surface (for each of the propellant mixes) are taken directly from the quench bomb data which measures the bi-modal particle size distribution at a distance of 0.5 inch from the burning surface.

Table IV. Discrete Phase Particle Properties

Parameter	Fine Al	Nominal Al	Coarse Al
Al_2O_3 Particle Density	100.0 lbm/ft^3	100.0 lbm/ft^3	100.0 lbm/ft^3
Al_2O_3 Caps Fraction	28.33%	28.33%	28.33%
Surface Particle/ Gas Velocity Ratio	0.85	0.85	0.85
Surface Particle Mass Mean Diameter	97.2	105.5	120.9
Surface Discrete Phase Fraction	37.71%	46.44%	48.42%
Surface Unburned Aluminum Fraction	22.15%	38.98%	42.39%

The surface unburned aluminum fraction in Table IV is calculated from the measured discrete phase fraction at the surface and the fixed value aluminum oxide caps fraction. The relationships between the local discrete phase fraction, the local unburned aluminum fraction and the fixed caps fraction are shown in the equations below. Equation (1) is a basic definition for the local discrete phase fraction which includes unburned aluminum in the particles. It states that the local discrete fraction is equal to the sum of the large Al_2O_3 particles and the unburned aluminum divided by the total of all the local condensed phase species including both the large and smoke Al_2O_3 particles and the unburned aluminum. Equation (2) follows from Equation (1) using the variables as defined below. Equation (3) is a rearrangement of Equation (2) in terms of the local unburned aluminum fraction.

$$f_p = \frac{\left(m_{Al_2O_3}\right)_p + \left(m_{Al}\right)}{\left(m_{Al_2O_3}\right)_p + \left(m_{Al_2O_3}\right)_s + \left(m_{Al}\right)} \qquad (1)$$

$$f_p = \frac{\beta * f_c * \left(1 - f_{Al}\right) + \left(f_{Al}\right)}{\left(f_{Al}\right) + \beta * \left(1 - f_{Al}\right)} \qquad (2)$$

$$f_{Al} = \frac{\beta * \left(f_c - f_p\right)}{f_p + \beta * \left(f_c - f_p\right) - 1} \qquad (3)$$

where

f_p is the fraction of discrete phase in the total condensed phase,

f_{Al} is the fraction of unburned aluminum in the total aluminum,

f_c is the fraction of burning aluminum converted to discrete phase Al_2O_3 (caps fraction) and

β is the mass ratio of Al_2O_3 to Al for complete combustion.

Measured data on the unburned aluminum fraction as a function of quench distance is shown in Figure 12 along with values calculated from equation (3) for a fixed caps fraction of 0.283 and using discrete phase fractions measured in the quench bomb for a 0.5 inch quench distance. The calculated values for unburned aluminum at 0.5 inch quench distance for the three mixes is shown to be in agreement with the data range. Furthermore, it can be seen that the unburned aluminum fraction is highest for the propellant mix with the coarse aluminum and lowest for the mix with the fine aluminum. A plot of the equation (3) relationship between the unburned aluminum fraction and the local discrete phase fraction is shown in Figure 13. Also shown are three points on the curve representing the boundary conditions at the propellant surface for the distributed combustion model in the CFD analysis for the three mixes analyzed.

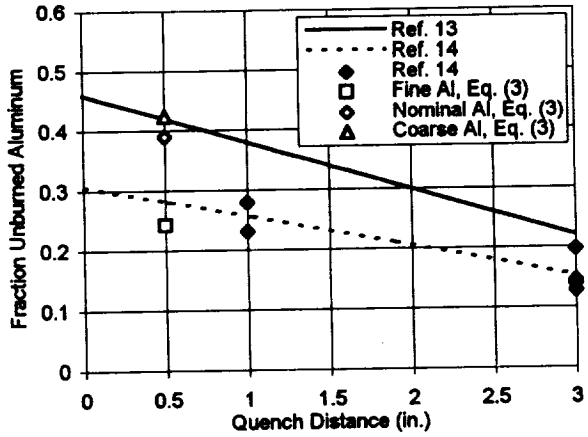

Figure 12. Unburned Aluminum Data/Analysis

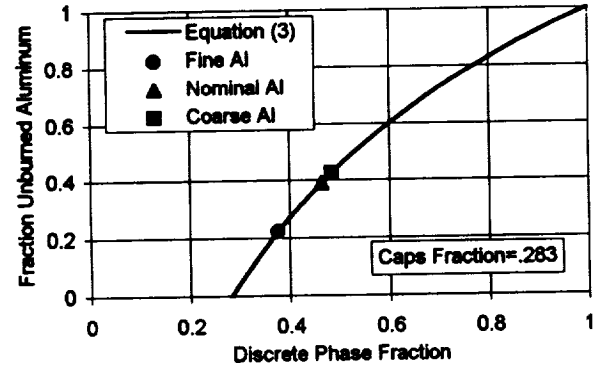

Figure 13. Calculated Unburned Al at Surface

Post-Test Analysis Results

Flowfield and Particle Trajectories

Flowfield solutions were obtained for each spin motor test condition at burn times representing 15, 50 and 85 percent web time. A representative velocity vector plot of the entire motor at 50 percent web is shown in Figure 14. It can be seen that the effect of mass addition down the port forces all of the mass generated in the

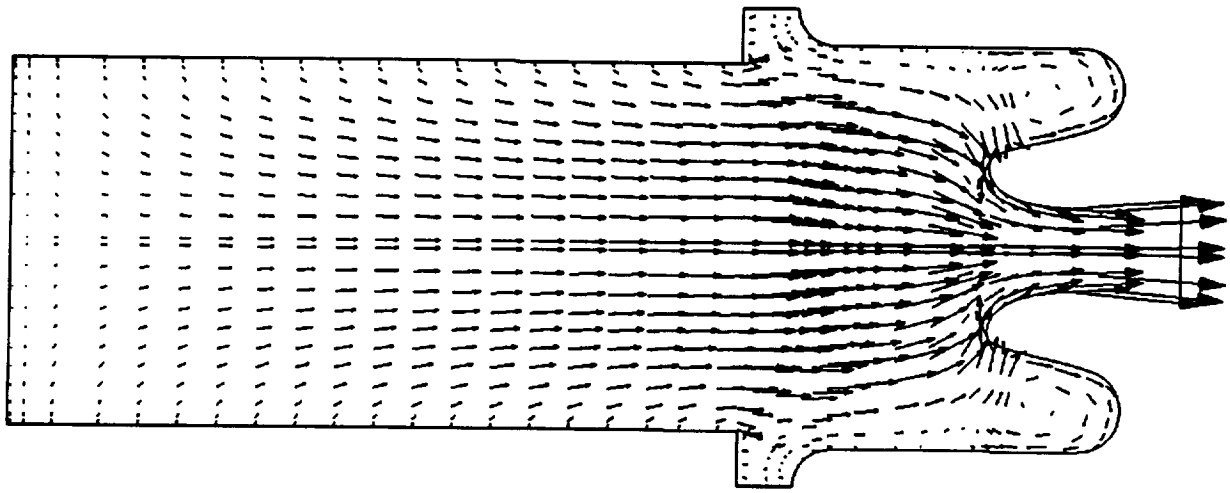

Figure 14. Spin Motor Velocity Vector Plot

head end of the motor toward the centerline and therefore only the flow generated in the aft end of the motor comes in contact with the aft closure and nozzle. Since the motor is spinning, the flowfield has a circumferential velocity component due to the conservation of angular momentum. A radial profile of the circumferential velocity component at the aft end of the propellant grain at 85 percent web time is shown in Figure 15.

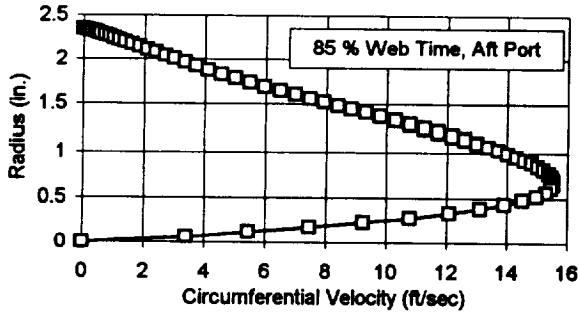

Figure 15. Spin Motor Circumferential Velocity

Trajectories for 200 micron particles at burn times of 15, 50 and 85 percent web time are shown in Figures 16, 17 and 18. These figures show that early in the burn only the end face of the burning propellant grain contributes to the particles captured underneath the nozzle and they are captured on the outer surface representing the case wall. At midburn, the particles from the end face are reduced and a portion of particles from the port flow are captured underneath the nozzle nose. Late in motor burn, a larger portion of the port flow particles are captured underneath the nozzle nose and the contribution from the end face of the grain has been reduced to small amounts on the forward end of the nozzle insert. The effect of 50, 100 and 200 micron particle sizes on the trajectories at 50 percent web time can be seen by comparing Figures 19 and 20 and the previously referenced Figure 17. The mass mean particle size is approximately 100 microns while the average size of the captured particles ranges up to 200 microns. However, particles of the 200 micron size that are generated in the forward end of the motor escape through the nozzle. It is clear from these figures that the slag collected in the aft region underneath the submerged nose is generated from propellant in the aft end of the motor.

Slag Accumulation

The particle mass impact rates per unit area were calculated from the two-phase CFD analysis by summing over the entire discrete phase particle distribution. These calculations were performed for Zones B, C and D for the submerged nose nozzle as shown in Figure 21. Slag was trapped in these zones by the nature of the nozzle design as well as the effect of motor spin. Slag measurements were recorded for these primary zones as well as the cylindrical motor chamber and the supersonic portion of the exhaust nozzle. All particles that impacted the surface downstream of the nozzle flow reattachment point were assumed to be permanently captured. This assumption is supported by the fact that the particles freeze on the surface which remains below the melting temperature of aluminum oxide due to the short burn time. However, all particles toward the nose tip from the flow reattachment point were

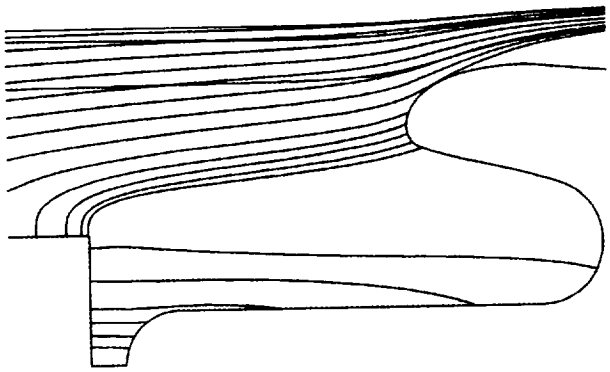

Figure 16. Trajectories of 200 Micron Particles at 15% Web Time

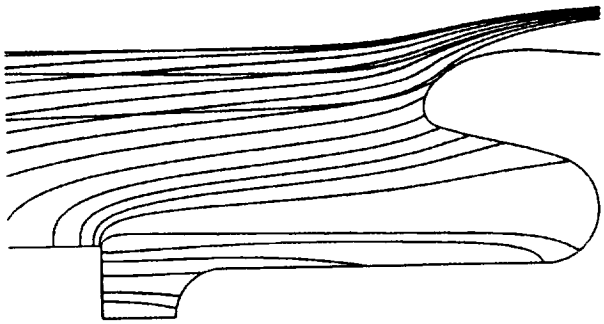

Figure 17. Trajectories of 200 Micron Particles at 50% Web Time

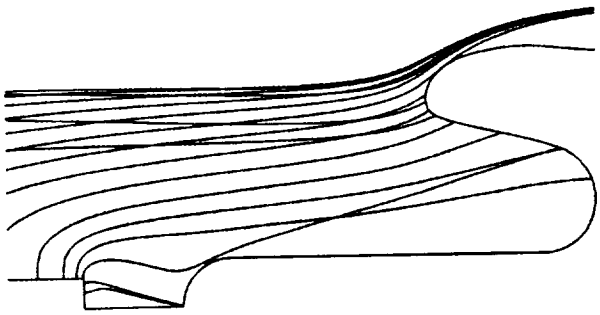

Figure 18. Trajectories of 200 Micron Particles at 85% Web Time

assumed to be swept out of the nozzle by the high velocity gasses. Thus the capture criteria used for this analysis is that all particles impacting the nozzle aft of the reattachment point are trapped as slag deposits and all particles impacting the nozzle forward of the reattachment point are swept out of the nozzle. This assumption is supported by the experimental results which showed that no slag deposits were observed around the nozzle nose tip. The slag accumulation rates for each of the major zones B, C and

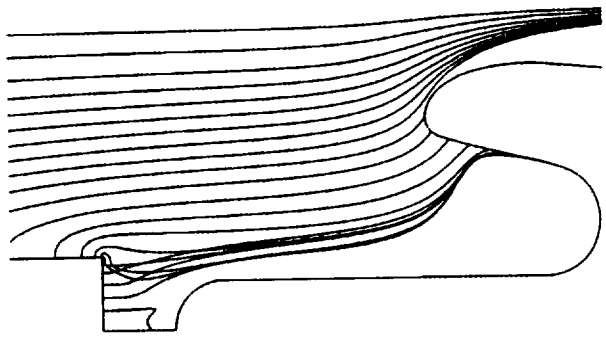

Figure 19. Trajectories of 50 Micron Particles at 50% Web Time

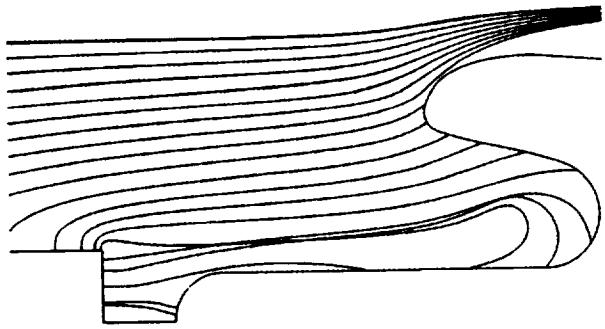

Figure 20. Trajectories of 100 Micron Particles at 50% Web Time

D are shown in Figure 22 as a function of percent motor web time for the nominal aluminum propellant. A curve of the total slag accumulation rate is also shown in Figure 22. It can be seen that most of the slag is accumulated in Zone B as expected from the flowfield and particle trajectory plots.

Total slag accumulation rates for nozzle Zones B, C and D were similarly calculated for the fine and coarse aluminum propellants, respectively. The slag accumulation rates for each of

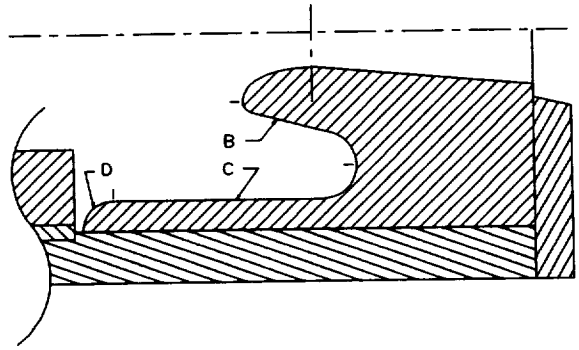

Figure 21. Spin Motor Slag Collection Zones

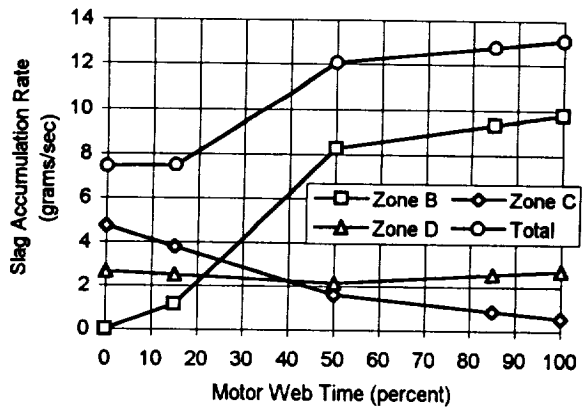

Figure 22. Slag Accumulation Rates, Nominal Al

the three propellants were then integrated with motor burn time to calculate a cumulative slag weight as a function of motor burn time. The results are shown in Figure 23. The coarse aluminum propellant yields the highest predicted slag weight at the end of motor burn followed by the nominal aluminum propellant with the fine aluminum propellant resulting in the lowest slag weight. The experimental data points for the measured slag weights of the three propellants are also plotted in Figure 23. Reasonably good agreement between the slag weight predictions from the two-phase CFD code and the measured data is evident. No special adjustments were made to the boundary conditions or input parameters to achieve these comparisons. The predictions are approximately 20 percent higher than the data but the predicted spread between the slag weight for the fine aluminum and the slag weight for the coarse aluminum is exactly correct. The predicted distribution of the slag over the submerged nozzle surface is compared with the measured data in Figure 24. The slag thickness

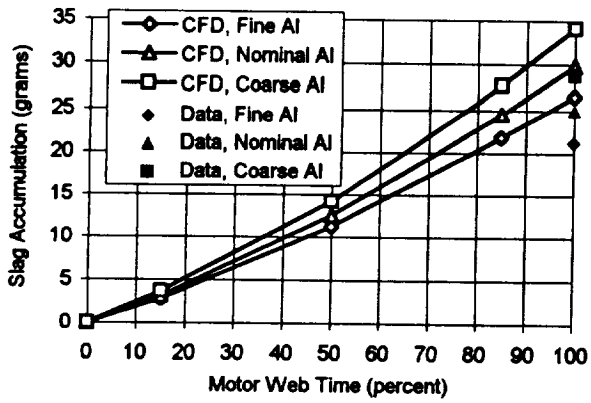

Figure 23. Total Slag Accumulation

dimension is amplified by a factor of four to facilitate visual comparison. An enlarged view of the highest slag weight zone immediately underneath the nozzle nose is shown in Figure 25. The two-phase CFD analysis compares favorably with the data in predicting the distribution of the accumulated slag over the underneath surface of the nozzle except at the forward edge of the slag layer. The CFD predictions and the measured data for the slag deposits are in good agreement as to the location of the edge of the slag deposit which supports the capture criteria assumption based on the location of the flow reattachment point. The predicted slag layer thickness is higher than the data at the forward edge due to shearing action on the deposit layer as evidenced by the thickness taper at the forward edge of the slag layer. This effect which is unaccounted for in the analysis may explain the slightly higher predicted slag weights.

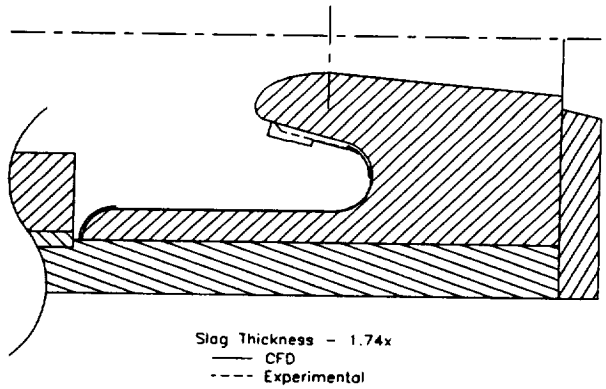

Figure 24. Spin Motor Nozzle Slag Deposits

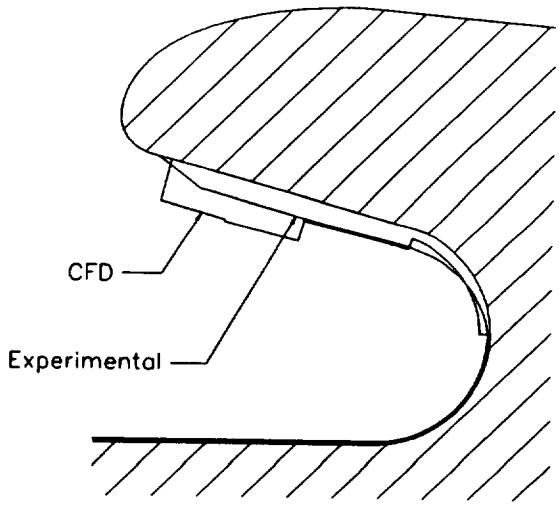

Figure 25. Spin Motor Nozzle Nose Slag Deposits

Conclusions

An experimental subscale motor and test program were designed to measure the relative propensity for slag production of propellants with relatively subtle ingredient variations. The use of a fully coupled two-phase fluid dynamic analysis was highly successful in gauging the viability of the experimental program during the critical initial planning phase before any data were available. Using flow analysis, a submerged nose nozzle was designed which replicated the dominant flow features of the submerged nose region in the full scale RSRM and enhanced the slag retention capabilities of the subscale nozzle. Also, the quantitative advantages of spinning the motor and the selection of the actual test spin rate were determined using a priori predictions from the fluid dynamics code. The initial predicted effects of spin on slag capture weights were later confirmed by the experimental data.

The two-phase distributed combustion model proved to be a credible analysis tool in evaluating the measured slag weight distributions in the 5-inch test motor. The fluid flow model correctly predicted the magnitude of the relative effect of measured quench bomb particle size distributions for various propellants on the slag weights collected in the test motor. The predicted values for absolute slag weights were approximately 20 percent higher than the measured values which is considered very close considering the lack of any arbitrary calibration constants in the model. The model predicted the highest slag weight for the coarse aluminum propellant and the lowest weight for the fine aluminum propellant.

The slag capture criteria is an important factor in the prediction model affecting predictions of slag weight. Use of the flow reattachment point underneath the nozzle nose in the slag capture criteria has physical significance for submerged nose nozzles where the flow splits at the attach location and goes forward toward the nose on one side and aftwards away from the nose on the other side of the attach point. Also, this criteria enables the two-phase fluid dynamics methodology used in the subscale motor to be applied to the full scale RSRM. Application of this methodology to slag predictions for the RSRM will be accomplished in the future although the relative magnitudes of the effects of propellant ingredient variations on captured slag weights are not necessarily expected to be the same as for the subscale motor. The trends, of course, are expected to be the same.

Acknowledgments

The efforts at ERC, Inc. on this project were performed under NASA Marshall Space Flight Center contract NAS8-40347. The authors would like to especially acknowledge the many contributions of NASA personnel who served on the Pressure Perturbation Team. The detailed design, manufacture and testing of the subscale motors was performed by Thiokol Corporation.

References

1. Schorr, A. A., and Speas, K. J, "Reusable Solid Rocket Motor (RSRM) Pressure Perturbation Characterization – An Overview," AIAA-95-2722, 31st AIAA Joint Propulsion Conference and Exhibit, San Diego, CA, July 10-12, 1995.

2. Sambamurthi, J. K., Price, E. W., and Sigman, R. K., "Aluminum Agglomeration in Solid Rocket Propellant Combustion," AIAA Journal, Vol. 22, No. 8, August 1984, pp. 1132-1138.

3. Miks, K. F. and Allen, A. S., "Effect of Propellant Variables on Slag in Subscale Spin Motors, Part II of III: Experiment Design, Execution and Results," JANNAF Propulsion Meeting, Tampa, FL, December 1995.

4. Perkins, F. M., May, D. H., and Beus, R. W., "Assessment of Propellant Relative Slag Potential by Direct Measurement of Slag in Sub-Scale Motors", AIAA-96-2781, 32nd AIAA Joint Propulsion Conference and Exhibit, Lake Buena Vista, FL, July 1-3, 1996.

5. Sabnis J. S., de Jong F. J., and Gibeling H. J., "Calculation of Particle Trajectories in Solid Rocket Motors with Arbitrary Acceleration", AIAA 91-3392, 27th AIAA Joint Propulsion Conference, Sacramento, CA, June 24-26, 1991.

6. Briley, W. R. and McDonald, H., "Solution of the Multidimensional Compressible Navier-Stokes Equations by a Generalized Implicit Method", Journal of Computational Physics, Vol. 24, August 1977, pp. 372-397.

7. Sabnis J. S., Madabhushi, R. K., and Gibeling H. J. and McDonald, H., "On the Use of k-ε Turbulence Model for Computation of Solid Rocket Internal Flows", AIAA 89-2558, 25th AIAA Joint Propulsion Conference, Monterey, CA, July 10-12, 1989.

8. Hermsen, R. W., "Aluminum Combustion Efficiency in Solid Rocket Motors", AIAA 81-0038, 19th AIAA Aerospace Sciences Meeting, St. Louis, MO, January 12-15, 1981.

9. Hunter, S. C., Cherry, S. S., Waldman, C. H. and Kliegel, J. R., "One Dimensional Reacting Three-Phase Flow with Mass Transfer Between Phases", Vol. 1-Final Technical Report, AFRPL-TR-81-103, April 1982.

10. Salita, M., "Use of Water and Mercury Droplets to Simulate Al_2O_3 Collision/ Coalescence in Rocket Motors", Journal of Propulsion and Power, Vol. 7, No. 4, 1991, pp. 505-512.

11. Miles, W., "The Effect of Altered Aluminum Powder Particle Size Distributions on Slag Generation in Subscale Spin Motors Containing Shuttle Main Grain Propellant," AIAA-96-3271, 32nd AIAA Joint Propulsion Conference and Exhibit, Lake Buena Vista, Florida, July 1-3, 1996.

12. Brennan, M., "Combustion Bomb Testing in RSRM Propellant," AIAA-96-3270, 32nd AIAA Joint Propulsion Conference and Exhibit, Lake Buena Vista, Florida, July 1-3, 1996.

13. Braithwaite, P. G., Christensen, W. N., and Daugherty, V., "Quench Bomb Investigation of Al_2O_3 Formation from Solid Rocket Propellants (Part I): Experimental Methodology," CPIA, 25th JANNAF Combustion Meeting, Oct. 1988.

14. Hutchison, B. J., Hoffman, T. R., Champneys, J. O., and Peterson, H. J., "Quench Bomb Testing on TP-H1148 Propellant," Thiokol Report TWR-65162, January 1994.

ASRM Subscale Plume Test

A subscale motor test to evaluate the effect of propellant ingredients on infrared plume radiation for both ASRM and RSRM type propellants was planned by ED33. A subscale graphite nozzle for this motor was designed by ERC. The design incorporated a steel nozzle body shell to contain the graphite insert and prevent the graphite from experiencing tensile stresses which may have caused longitudinal cracking observed on earlier tests with this motor. The nozzle expansion section is a scaled ASRM contour and the contraction section is a hyperbolic spiral extending forward to which it becomes tangent to a 40.57 degree entrance ramp angle. A design layout was provided to ED33 with detailed component design to be completed in June. The design layout was documented as ERC drawing H4500. The detailed engineering drawings are H4501 for the top level assembly and H4502 for the nozzle component part details. The design consists of a graphite insert pressed into a steel nozzle body which slides into the motor case with an o-ring seal. This design holds the graphite in compression to prevent the graphite from experiencing tensile stresses which may have caused the longitudinal cracks observed on earlier tests with this motor which used a graphite insert with a loose fit into the motor case.

A thermal analysis of the ASRM subscale nozzle exit cone was performed to determine the possibility of surface melting of the steel section (see ERC Dwg. No. H4500). This analysis was performed using the Reaction Kinetics Ablation Program (REKAP), which has the capability of modeling one-dimensional, time-dependent heat transfer in multilayered, decomposing materials with surface recession. While this code contained may more capabilities than required for this analysis, it is easily used to model non-ablating materials with time dependent convective and radiative heating.

The nozzle exit cone was axisymmetric, so a rigorous solution of the steel portion could be obtained with a 2-D model of the graphite and steel. However, an approximate solution is easily obtained with a 1-D (radial) analysis through the steel. The graphite will conduct some heat into the steel; however, by using the location of highest heating of the steel (at the interface, I. D. = 5.958 in) and eliminating the heat sink capacities of the motor case and spring pins (no heat transfer at these interfaces), the analysis is probably conservative. The 0.90-in thickness of 4130 steel at the steel-graphite interface is modeled using cylindrical coordinates to account for radial effects. Heating from the inside occurs from gaseous convection and particulate radiation (predominately aluminum oxide), while the outside surface (the interface) is adiabatic.

The heating environment on the inside surface uses 1) thermochemical properties from TRAN72 predictions, 2) convective film coefficients computed using a Bartz short form analogy, and 3) radiation computed from a gaseous cloud of gray particles (Al_2O_3). Thermochemical properties computed at the exit for a chamber pressure of 580 psia include:

T_o	=	6345°	(stagnation temperature)
M	=	30.785 lbm/lb_{mole}	(molecular weight)
γ	=	1.1455	(specific heat ratio)
$W_{condensed}$	=	0.386	(weight fraction of condensed species)
$C_{pfrozen}$	=	.4509 BTU/lbm°R	(specific heat)
C*	=	5158 ft/sec	(characteristic velocity)
C	=	2795.5 ft/sec	(local sonic velocity)

These properties and others are used to compute Bartz film coefficients, which are time dependent since the temperature-dependent properties (viscosity, thermal conductivity and density) are continuously updated as the steel surface temperature increases. The Bartz short form analogy has proven for many years to be very adequate when used with REKAP and the gray cloud radiation model.

The gray cloud radiation model has been effective for exhaust plumes of aluminized propellants if a good estimate of the particle temperature can be obtained. Because of the two-phase lag of the particle temperatures, a good estimate is difficult, especially in the exit cone where gas temperatures are dropping rapidly. For the purposes of this analysis, two extremes were chosen. The maximum temperature that the particles could be is the local recovery temperature, which is 6,012°R. The lowest possible temperature (because of two-phase temperature lag) is the local gas temperature, which is 4,167°R. Using an individual particle emissivity of 0.17 and a particle density of 140 lbm/ft^3, radiation heat fluxes of 263.0 and 60.7 BTU/ft^2sec are computed. The actual flux should lie somewhere between these - probably between 100 and 200. However, for this analysis, the broader range was used.

When these boundary conditions were applied to the REKAP model, the results of Figures 1 through 4 were obtained. Figures 1 and 3 represent the predicted surface and interface temperature histories using the two radiation values. The maximum 4130 steel surface temperature at web time (5.0 sec) is 2,352°F (Figure 1), which is still well below the 2750°F melting point. The actual maximum value of surface temperature is probably closer to the lower number of 1750°F. Also, the interface maximum temperature should be between 172 and 307°F or less because of the conservative adiabatic surface assumption. These low temperatures should cause no physical property degradation of the shear-pins or bearing surface, and the o-ring groove located forward of this location should not be adversely effected.

Figures 2 and 4 represent the heat flux values for two radiation levels. The total heat flux is the sum of the convection and net radiation fluxes. The net radiation flux is the incident gray cloud radiation decremented by the re-radiation from the heated surface. The convective film coefficients (Bartz) are affected by the surface temperature and must be computed for the predicted surface temperature response. This is obviously

an iterative procedure. The final enthalpy-based Bartz film coefficients in units of lbm/ft^{2}sec are as follows:

time (sec)	$h/C_p)_1$	$h/C_p)_2$
0.0	0.0	0.0
0.01	0.229	0.229
0.5	0.203	0.209
1.0	0.195	0.203
2.0	0.187	0.195
3.0	0.182	0.191
4.0	0.178	0.188
5.0	0.175	0.186

The computer code used to perform this analysis was converted to an IBM PC compatible version from an IBM mainframe version. The source code on a 9 track tape was converted to floppy disk DOS format and recompiled on a Lahey compiler and checked out with several test cases. The code is REKAP (Reaction Kinetics Ablation Program) and will handle transient charring and ablation materials. This effort was performed by a consultant, W. C. Aycock. The code will prove useful in interfacing CFD and aerothermal concerns for subscale motors as well as ASRM.

Figure 1. Temperature Histories Using Higher Radiative Flux

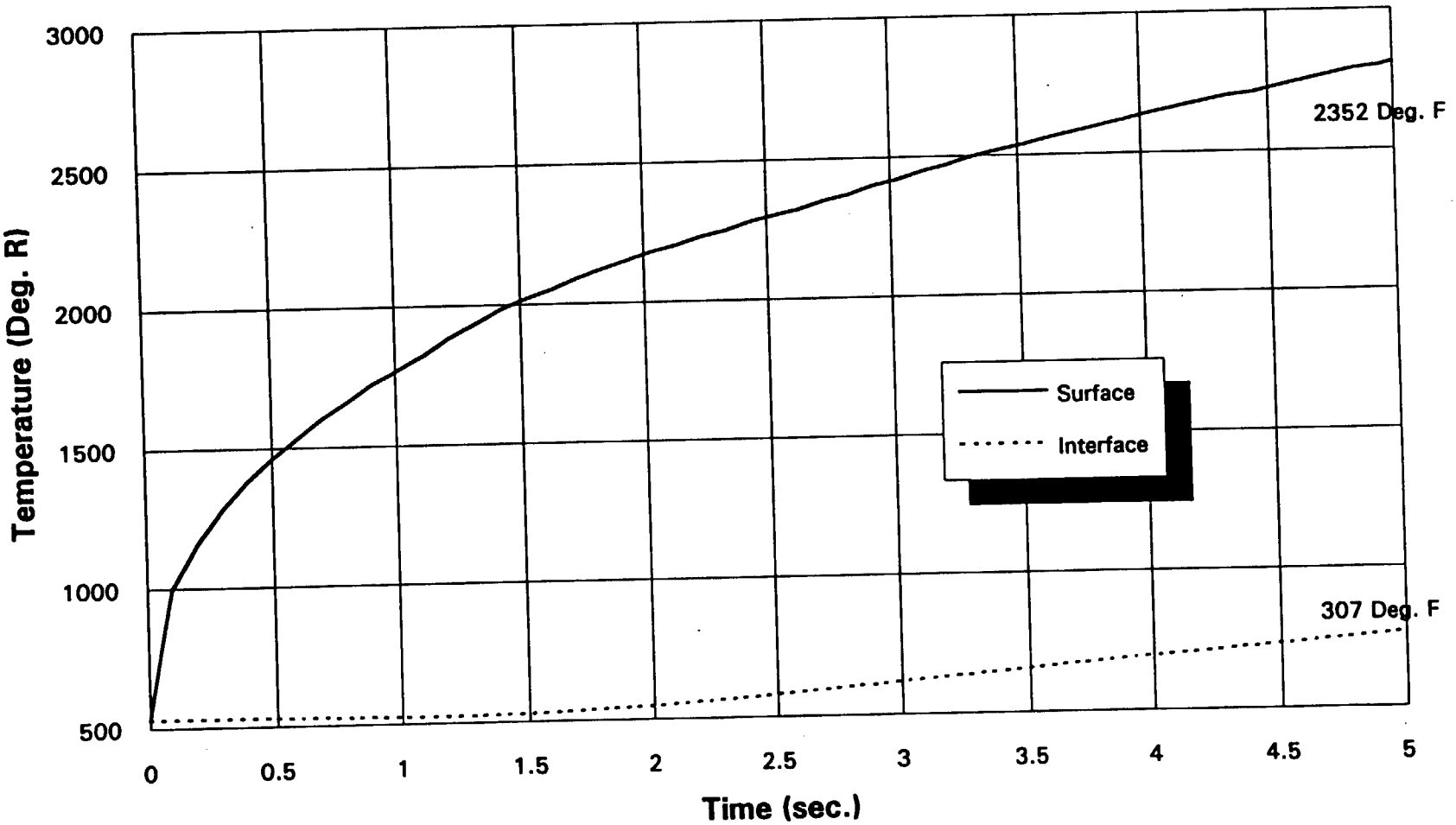

ERCI 07/14/92

Figure 2. Heat Flux Histories Using Higher Radiative Flux

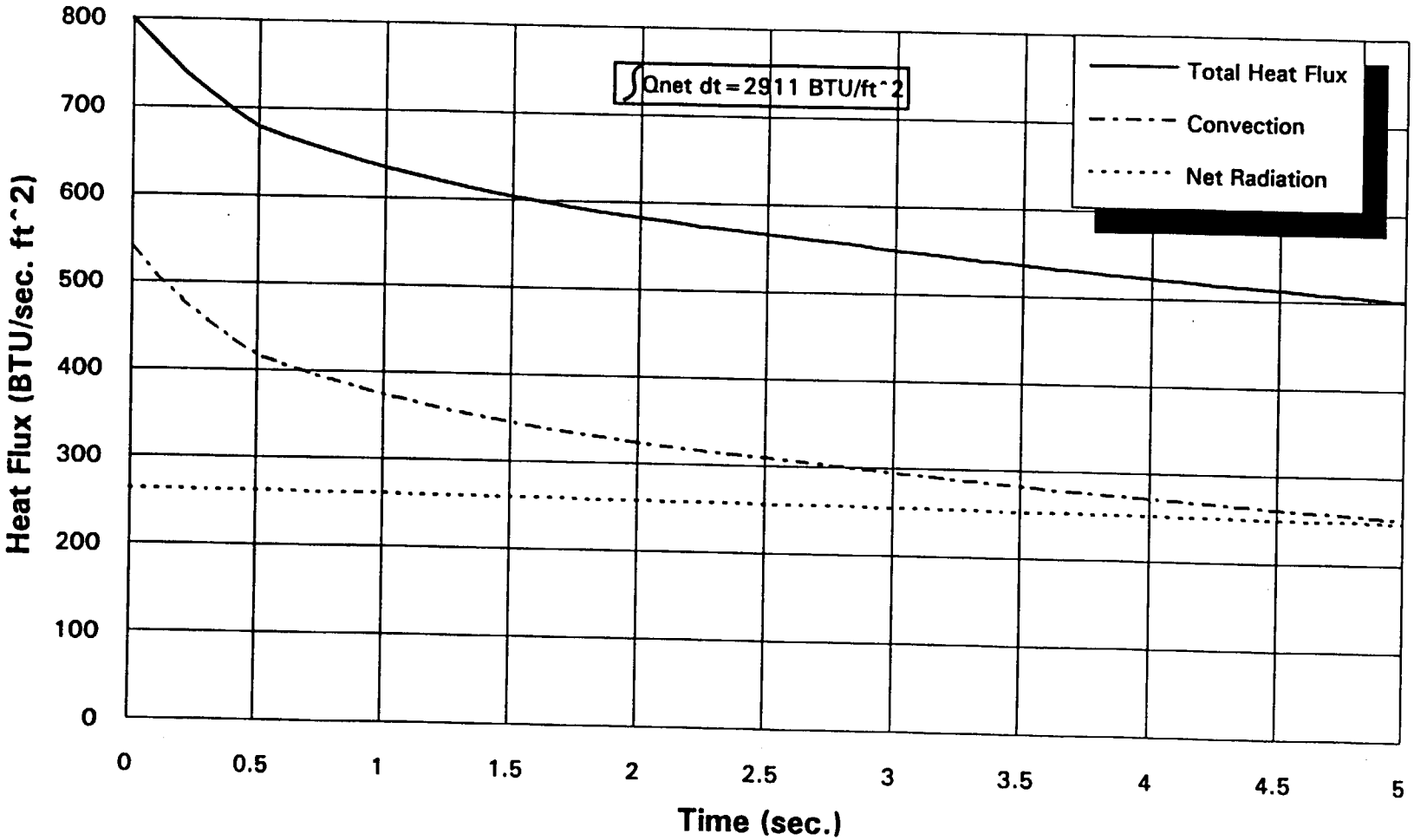

ERCI 07/14/92

Figure 3. Temperature Histories Using Lower Radiative Flux

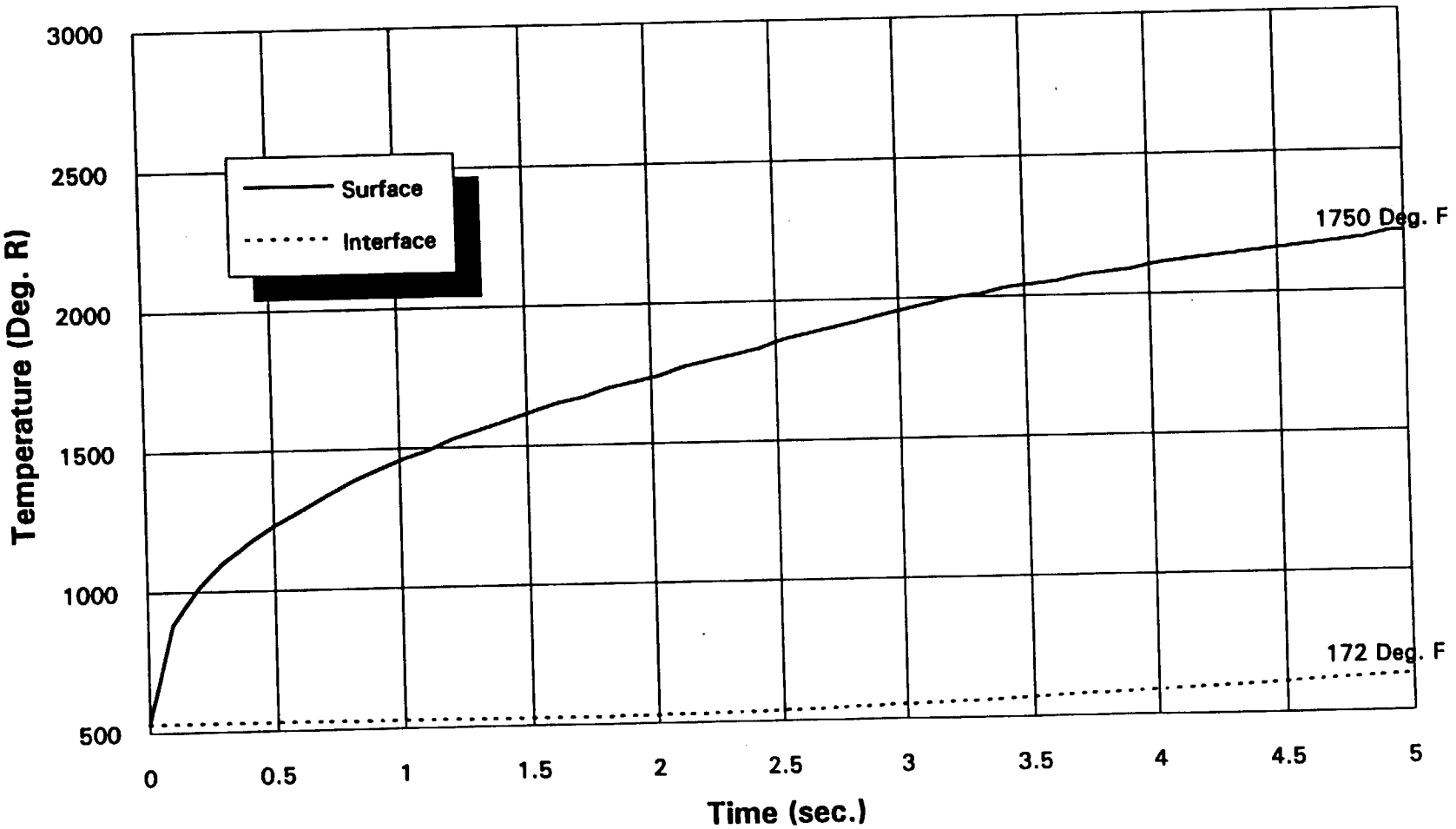

ERCI 07/14/92

Figure 4. Heat Flux Histories Using Lower Radiative Flux

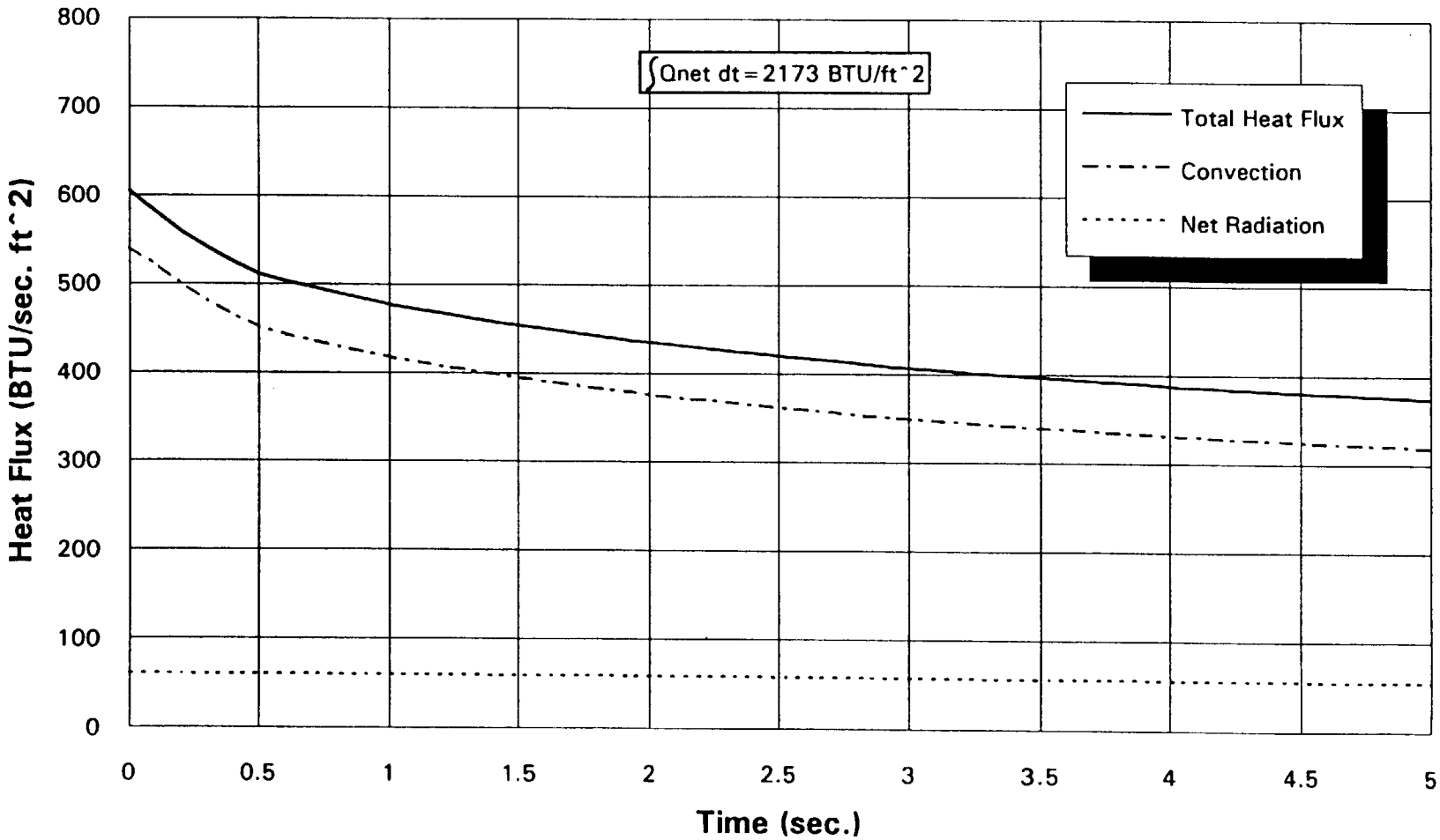

ERCI 07/14/92

NASA-MSFC